Substitution-Mediated Calcination of Nickel-Based Cathodes: Decoupling Lithiation and Crystallization

*Pallab Barai[1, #], Sizhan Liu[2, #], Juan C. Garcia[1], Xiaoping Wang[1], Ozgenur Kahvecioglu[1], Krzysztof Z. Pupek[1, ♦], Venkat Srinivasan[1], Hakim Iddir[1], Jianming Bai[2, *], Feng Wang[1, *]*

1. Argonne National Laboratory, Lemont, IL 60439, USA

2. Brookhaven National Laboratory, Upton, NY 11973, USA

KEYWORDS: Lithium-ion batteries; Nickel-based layered cathodes; Calcination; Lithiation; Layering; Crystallization; In situ characterization; Multiscale modeling

ABSTRACT: Nickel-based layered cathodes such as $LiNiO_2$ offer high energy density for lithium-ion batteries, yet improvements in cycling performance and safety are required for practical use – often achieved through manganese and cobalt substitution, as in $LiNi_{0.80}Mn_{0.10}Co_{0.10}O_2$ (NMC811). However, how such substitution impacts calcination, the key process governing lithiation, structural ordering, crystallization, and ultimately the resulting material properties, remains unclear. Here, we investigate substitution-mediated calcination dynamics in NMC811 compared to $LiNiO_2$ using multiscale-correlated *in situ* spectroscopy and atomistic-to-mesoscale modeling. While both systems progress through a common sequence of intermediates toward the thermodynamically favored layered phase, NMC811 exhibits an earlier onset of layering concurrent with hydroxide decomposition, followed by sluggish crystallization. Modeling reveals that Mn and Co lower the energy barrier for lithium incorporation and ordering but increase the penalty for interlayer gliding, thereby slowing crystal growth at elevated temperatures. This substitution-mediated decoupling of lithiation and crystallization explains the fine-grained microstructure observed in NMC811 *versus* coarsened particles in $LiNiO_2$ and establishes a mechanistic framework for predictive microstructure engineering of Ni-based cathodes.

1. Introduction

Transition metal (TM) oxides represent a versatile family of materials widely used in optics, electronics, catalysis, and energy storage owing to their abundance, structural diversity and tunable properties.[1-4] Among them, nickel (Ni)-based layered oxides have emerged as cornerstone cathode materials for high-energy lithium-ion batteries (LIBs), offering high specific capacities while reducing reliance on cobalt.[5-7] To further boost storage capacity, research efforts have increasingly focused on cathodes with higher Ni content. However, increasing Ni concentration exacerbates detrimental phenomena such as cation mixing, surface reactivity, and particle cracking, which compromise long-term performance.[8] Stoichiometric $LiNiO_2$ (LNO), the pure Ni endmember, offers the highest theoretical capacity among Ni-based cathodes, but suffers from poor cycling and thermal stability.[9-11] Its synthesis presents an additional hurdle: slight deviations from the ideal $LiNiO_2$ stoichiometry lead to Li deficiency ($Li_{1-z}Ni_{1+z}O_2$) and Ni^{2+} occupancy of Li sites, further compromising performance.[12] These complexities have historically hindered the practical adoption of LNO.[13] Partial substitution of Ni with Mn and Co is a well-established route to stabilize Ni-based cathodes as exemplified by commercialized $LiNi_{0.80}Mn_{0.10}Co_{0.10}O_2$ (NMC811).[14-16]

Ni-based cathode materials are typically synthesized *via* two major steps: coprecipitation and calcination. Coprecipitation defines the precursor composition and morphology, establishes primary and secondary particle architectures, and enables homogeneous elemental distribution or compositional gradients. The subsequent calcination step dictates the lithiation, structural ordering, crystallization, and thus ultimately determines the microstructure and electrochemical performance of the synthesized cathode materials.[13, 14] Calcination is inherently complex, involving intercoupled processes, including dehydration, oxidation, lithiation, and structural transformation, collectively dictating phase progression and crystallization.[12, 15] Subtle variations in calcination parameters, such as temperature, duration, or atmosphere, can significantly alter the resulting microstructure and performance.

Elemental substitution provides additional control over the structural transformations during calcination. Co substitution not only enhances electronic conductivity, which is essential for cycling, but also promotes structural ordering during calcination.[16] Mn, by contrast, has been shown to influence microstructural development during the sintering process by suppressing the migration of grain boundaries in addition to its well-established roles of stabilizing the layered structure during cycling.[17] The combined use of both Mn and Co is therefore widely applied to maintain structural integrity of Ni-based cathodes, enabling both high capacity and long cycling stability.[18, 19] Despite their widespread use, the mechanistic roles of Mn/Co substitution during calcination – particularly how they regulate lithium incorporation (lithiation), layered-phase formation (layering), and crystallization, remain poorly understood. [21-24]

In our recent study, we demonstrated the intricate interplay between thermodynamics and kinetics during calcination of LNO, particularly the intercoupling of lithiation, layering, and crystallization.[21] For example, concurrent lithiation and dehy-

dration occurred in LNO, resulting in low-temperature crystallization of the layered phase alongside lithiated rocksalt intermediates. The calcination process is strongly composition-dependent: Mn and Co substitution alter lithium incorporation, structural ordering, and phase-transition pathways, ultimately yielding markedly different microstructures and morphologies (**Scheme 1**).[25-28] However, a detailed mechanistic understanding of how Mn and Co regulate the calcination of Ni-based cathodes, in terms of intermediate phase formation, lithium diffusion, transition metal migration, and grain growth – remains elusive.[29-32]

To address this knowledge gap, we investigate how Mn and Co substitution impacts the sequence and kinetics of phase progression and crystallization during the calcination of Ni-based cathodes, using two model systems, NMC811 and LNO. Correlated *in situ* X-ray diffraction and total scattering coupled with pair distribution function (PDF) analysis, are employed to capture the structural evolution of intermediates, both short and long-range order. Our results show that, while both systems undergo similar processes towards the thermodynamically-favored layered phase, NMC811 exhibits an earlier onset of layering, followed by a slower layered-phase crystallization compared to LNO.

To rationalize these observations, we perform atomistic modeling and phase field-based continuum simulations to capture key chemical reactions (dehydration, oxidation, lithiation, layering) and sintering processes (mediated by surface, grain-boundary, and bulk diffusion mechanisms).[33-34] This integrated atomistic-to- mesoscale modeling reveals that Mn and Co substitution facilitates low-temperature lithiation and layering, while imposing a high energy barrier that inhibits gliding between transition metal and lithium layers, thereby slowing the growth of the layered phase at elevated temperatures. This substitution-mediated decoupling of lithiation and crystallization explains the observed distinct microstructures: fine-grained, porous secondary particles in NMC811 versus dense, coarsened grains in LNO. These findings establish a mechanistic framework for designing calcination strategies to control microstructure and optimize the electrochemical performance of Ni-based cathode materials.

2. Experimental Section

2.1 Synthesis of LNO and NMC811. $Ni(OH)_2$ and $Ni_{0.80}Co_{0.10}Mn_{0.10}(OH)_2$ (NMC811$(OH)_2$) precursor powders were continuously synthesized via coprecipitation, using a 10 L Taylor Vortex Reactor (TVR). The starting solutions consisted of 2 M of transition metal sulfate solutions with nominal Ni, Mn and Co ratios, along with 4 M NaOH and 4 M NH_4OH. Both $Ni(OH)_2$ and NMC811$(OH)_2$ coprecipitations were carried out with a 4-hour residence time. Prior to pumping the reactants into the reactor, the reactor was filled with nitrogen-purged deionized (DI) water, and the inner cylinder was rotated at 800 rpm for $Ni(OH)_2$ and 1250 rpm for NMC811$(OH)_2$ syntheses. The pH and temperature of the reaction were maintained at 12.00 (±0.02) and 50.00 ºC (±0.10ºC) for the $Ni(OH)_2$ reaction and at 11.10 (±0.05) and 42.00°C (±0.05 ºC) for NMC811$(OH)_2$. All reactants were pumped simultaneously, with NaOH flow controlling the pH. Once steady-state conditions were reached, the precipated hydroxides were collected with a rate of ~200 g/h continuously up to the desired amounts. The products were washed with nitrogen-purged DI water until the conductivity of the solution dropped below 20 μS/cm, then filtered, and dried overnight at 120 ºC in a vacuum oven.[35] For preparing the layered NMC oxides, the dried hydroxide precursors were mixed with Li source, $LiOH{\bullet}H_2O$ 5% with Li excess, and subjected to various in situ and ex situ calcination experiments.

2.2 *In Situ* High-Energy XRD Measurements. Correlated *in situ* high-energy X-ray diffraction and total scattering experiments were carried out at beamline 28-ID-2 of the National Synchrotron Light Source II (NSLS-II) at Brookhaven National Laboratory (BNL), as schematically illustrated in **Figure 1**(a). A monochromatic X-ray beam with a wavelength of 1.666 Å and a spot size of 0.5 mm (horizontal) × 0.5 mm (vertical) was used. The pellet sample was prepared from a mixture of $TM(OH)_2$ and $LiOH{\bullet}H_2O$ powders, at a molar ratio of 1.00: 1.05. The pellet was placed inside a vertically mounted furnace (Linkam TS 1500), with an open window aligned perpendicular to the X-ray beam. The pellet sample was heated at 20 °C steps from 35 °C to 1000 °C based on the furnace control temperature; see the heating profile given in **Figure 1**(b). At each temperature, the sample was held for about 5 minutes to ensure thermal equilibrium before taking in situ XRD patterns with 30-second counting time. A Perkin-Elmer XRD 1621 digital imaging detector was used to collect XRD patterns. A temperature calibration curve correlating the sample temperature to the control temperature was obtained by measuring the thermal expansion of CeO_2 under identical experimental conditions.

2.3 Refinement of XRD Data. Rietveld refinements of XRD patterns were carried out using the TOPAS-Academic software. $TM(OH)_2$ (SG: *P*-3*m*1), $Li_xTM_{2-x}O_2$ (SG: *Fm*-3*m*), and $LiTMO_2$ (SG: *R*-3*m*) were employed as the structural models for initial hydroxides, intermediates, and final layered oxides, respectively. $Li_xTM_{2-x}O_2$ is used here to describe the stoichiometry of lithium transition-metal (TM) oxides. This formulation unifies both the pure rocksalt phase, represented by x = 0 (with a normalization factor of 2), and the stoichiometric layered phase $LiTMO_2$, corresponding to x = 1. The parameter *x* directly corresponds to the Li occupancy at the 3b sites obtained from Rietveld refinement and represents the lithium content per $LixTM_{2}–xO_2$ formula unit, or per two rocksalt (Li, TM)O formula units.The global refining parameters included background coefficients, peak shape parameters, lattice parameters, and the weights of different structures. For the structure of the layered oxide, the positional parameter of O (6c); the fractional factors of all Li and TM and isotropic atomic displacement parameters (U_{iso}) were refined. The chemical formula $(Li_{1-x}TM_x)_{3b}(TM)_{3a}O_2$ was followed. That is, the total occupancy of Li and TM at 3b is 1. The U_{iso} of all elements sharing the same crystallography position was set to be equivalent.

2.4 *In situ* High-Energy X-ray Total Scattering Measurements and Pair distribution function (PDF) Analysis. Total scattering data sets were collected using Perkin Elmer Area detectors with a sample to detector distance of ~200 mm, simultaneously with XRD measurements (Figure 1(a)). Exact detector to sample distances were derived by fits to Ni powder calibration standards. The Ni standard was also used to determine setup specific parameters (Q_{damp} and Q_{broad}), which were held fixed for these samples. The range Q_{mim} = 0.2 $Å^{-1}$ and Q_{max} = 24.0 $Å^{-1}$ was used in data reduction. The sample information is the same as that in XRD measurements. Scans were collected with blank capillaries to determine the background scattering. This

background was subtracted from all datasets. The methods utilized for analysis of the PDF data are described in detail in Ref. 36. For the fits in R-space, the range $1.5 < r < 30$ Å was utilized.

The PDF G(r) is the reduced atomic pair distribution function which oscillates about zero and is obtained directly from the scattering data, $S(Q)$, with $Q = \frac{4\pi \sin(\theta)}{\lambda}$. The function $G(r) = \frac{2}{\pi}\int_{Q_{min}}^{Q_{max}} Q(S(Q)-1)\sin(Qr)\,dQ$ is related directly to the standard pair distribution function $g(r)$. $G(r) = 4\pi r\rho_0(g(r)-1)$, where ρ_0 is the number density of atoms. $F(Q)$ is defined as $F(Q) = Q(S(Q)-1)$. The PDF $G(r)$ includes all of Q-space between the limits of the integral in Q-space and not just at the peak positions. Hence, it captures the diffuse scattering.[37]

2.5 Atomistic Modeling Methodology The calculations were performed within the spin polarized density functional theory (DFT) methodology as implemented in the Vienna Ab Initio Simulation Package (VASP).[38-39] The generalized gradient approximation (GGA) is used to model the exchange-correlation potentials as developed by Perdew, Burke, and Ernzerholf (PBE).[40] The interaction between valence electrons and ion cores is described by the projected augmented wave (PAW) method.[41] Furthermore, the GGA+U scheme is used for applying the on-site correlation effects among 3d electrons of the transition metals, where the parameter of (U−J) is set to 6.20, 3.32, and 3.90 eV for Ni, Co, and Mn, respectively.[42] The magnetization was used to assign the oxidation state of the ions.

2.6 Multiscale Computational Methodology A phase-field-based computational modeling framework was developed at the mesoscale level to capture the sintering and chemical reaction (dehydration, oxidation, and lithiation) of the cathode active particles, as well as the evolution of the layered phase within the lithiated domains.[6] A Cahn-Hilliard type fourth-order partial differential equation was solved to capture the evolution of the conserved solid phase during the sintering process.[43] Grains are represented by non-conserved order parameters, and their growth was modeled by solving the Allen-Cahn type second-order partial differential equations. All three chemical reactions, namely, dehydration, oxidation, and lithiation of the cathode active particles were assumed to occur through a two-step process:[44]

a) reaction at the particle surface, and
b) subsequent transport of the species within the bulk of the active particles.

The movement of water and lithium was assumed to occur through a single-phase diffusion process, whereas the transport of oxygen was assumed to be a two-phase diffusion phenomenon (details provided in SI). Evolution of the layered phase occurred through the nucleation and growth of the layered domains within the lithiated phase.[45] Dehydration, oxidation, and lithiation induced volume expansion and subsequent stress evolution-driven viscoplastic deformation of the cathode particles were also captured by solving the equilibrium equation within the developed computational framework. Further details of the computational techniques and parameters used for running the simulations are provided in the Supplementary Information (SI).

For the calcination of NMC811 and LNO cathode particles, a temperature ramp protocol consistent with the experimental conditions was adopted. The temperature was raised from room temperature (RT; 25°C) up to 900 °C at a rate of 20°C/min for 1 minute and then held constant for 5 more minutes.

In situ X-ray diffraction analysis of the calcination process reveals that the hydroxide precursors for both NMC811 and LNO demonstrate average primary particle size around 10 nm. For the computational analysis, a microstructure containing randomly distributed particles with average size around 8 nm was generated and used as the initial particle microstructure at the beginning of the calcination process. The same initial microstructure was used for simulating the calcination of NMC811 and LNO cathode precursors. Dehydration, oxidation, lithiation, volume expansion, sintering, and subsequent layered phase formation were all simulated on these microstructures.

3. Results

3.1 Substitution-Mediated Phase Progression

Results from synchrotron XRD and scanning electron microscopy (SEM) analyses of the synthesized hydroxides and final layered oxides are provided in the SI (Figures S1–S4). The initial hydroxides, $Ni(OH)_2$ and $Ni_{0.8}Mn_{0.10}Co_{0.10}(OH)_2$, consisting of needle-like primary particles with a trigonal structure (space group: P-3m1), transformed into larger particles with a hexagonal layered structure (space group: R-3m) upon calcination. Significant structural and morphological changes occur during this process due to the involved dehydration, lithiation, structural ordering, and crystallization (illustrated in **Scheme 1**).

A comparison of particle size distributions and surface areas for $Ni(OH)_2$ and $Ni_{0.8}Mn_{0.10}Co_{0.10}(OH)_2$ precursors is shown in Figure S5. The two precursors exhibit comparable primary particle sizes and anistropic crystal growth, with average values of 11.3 nm for $Ni_{0.8}Mn_{0.10}Co_{0.10}(OH)_2$ and 15.4 nm for $Ni(OH)_2$, being estimated by the Scherrer equation. Brunauer–Emmett–Teller (BET) surface area measurements also indicate similar values: 20.6 m^2/g for $Ni_{0.8}Mn_{0.10}Co_{0.10}(OH)_2$ and 16.4 m^2/g for $Ni(OH)_2$. The slight differences in particle size and surface area are primarily attributed to the lower co-precipitation temperature used for $Ni_{0.8}Mn_{0.10}Co_{0.10}(OH)_2$ (42 °C) compared to $Ni(OH)_2$ (48 °C).

To elucidate the substitutional effects of Mn and Co, *in situ* synchrotron XRD and PDF data were collected simultaneously during calcination of NMC811 and LNO. These measurements enabled tracking of intermediates and their structural evolution, from the long-range order down to local octahedral units.[22] The overall phase transformation trends are illustrated by the contour plots of the temperature-resolved XRD patterns (Figure S6). A zoom-in view of the low-angle diffraction region is provided in Figures 1c-e to highlight the contrasting structural evolution of the two systems. In NMC811, the $(003)_l$ peak, characteristic of the layered phase, emerged early, upon the hydroxide decomposition, indicating that Mn and Co substitution promotes early-stage layering.[22] While LNO exhibited a significantly delayed appearance of the layered phase, with the $(003)_l$ reflection only developing at much higher temperatures.

To quantify the major phases evolving during calcination, Rietveld refinements were applied to individual *in situ* XRD patterns, capturing contributions of distinct phases to subtle features, such as asymmetric shoulders. Representative calculated patterns compared with experimental data are shown in **Figure S7**. Refined Structural Parameters are provide in **Tables S1-S3**. The phase progression of NMC811 and LNO with temperature, as summarized in Figure 1(f), can be categorized into four sequential stages: I (RT to ~180°C), II (180-280°C), III (280-650°C), and IV (above 650°C):

Stage I (below 180°C). No new Bragg peaks emerged beyond those from hydroxide precursors, indicating that the layered hydroxide structure (*P*-3*m*1) was largely preserved. However, anisotropic lattice expansion occurred, as evidenced by the gradual shift of the $(001)_P$ peak to lower angles as temperature increased (Figure 1 (d, e)).

Stage II (180-280°C). This stage marks the onset of dehydration and early lithiation, accompanied by an abrupt phase transition with multiple co-existing intermediates. In LNO, the Bragg peak $(001)_P$ continuously shifted to lower angles due to thermal expansion (Figure 1(e)). In NMC811, the Bragg peak $(001)_P$ first shifted to lower and then to higher angles before rapidly disappearing, indicating lattice shrinking as a result of faster dehydration. Simultaneously, the $(003)_L$ characteristic of the layered phase (at ~2.01°) appeared together with rocksalt reflections, coinciding with the disappearance of hydroxide peaks (Figure 1(d)). Notably, in LNO, the appearance of the characteristic $(003)_L$ was significantly delayed, highlighting that Mn and Co substitution facilitates early lithiation and rapid initial layering in NMC811. By the end of this stage, hydroxide phases were fully consumed (Figure 1(f)).

Stage III (280-650°C). Lithiated rocksalt $Li_xTM_{2-x}O_2$ gradually converted into to the layered phase ($LiTMO_2$). In LNO, the $(003)_L$ peak emerged at ~330°C, but remained weak and broad, reflecting delayed nucleation of nanoscale layered domains and concurrent lithiation of the rocksalt lattice (evidenced by peak shifts to higher angles). Although layered domains formed earlier in NMC811, the conversion of lithiated rocksalt to the layered phase progressed more slowly in NMC811 than in LNO (Figure1(f)), suggesting that Mn and Co substitution slows crystallization, despite promoting early layering.

Stage IV (above 650°C). Both LNO and NMC811 underwent rapid rocksalt-to-layered phase transformation, accompanied by pronounced crystallite growth, as reflected by the dramatic increase in $(003)_L$ peak intensity (Figure1(d, e)). Despite its earlier onset of layering, NMC811 exhibited notably slower growth of the layered phase compared to LNO; the rocksalt-to-layered phase transformation reamined incomplete even at the end of the in situ experiment (~ 865°C), further confirming the crystallization-inhibiting effect of Mn and Co substitution at high temperatures. As shown in Figure1(f), Li_2CO_3 formation occurred in both systems due to the exposure to ambient air and may have slowed the lithiation process (see detailed discussion in the SI; **Note S1**).

The phase progression in LNO and NMC811 was further examined using thermal gravimetry analysis (TGA) and differential scanning calorimetry (DSC), revealing distinct behaviors between the two systems (Figure S8). Due to Mn and Co substitution, the onset of water loss from $LiOH.H_2O$ in the mixture with $NMC811(OH)_2$ shifted to lower temperatures (at ~ 79.6 °C) compared to the $Ni(OH)_2$ mixture (~ 87.5°C). In both cases, dehydration of $Ni(OH)_2$ occurred between 200 and 320°C, as observed in the DSC curves. Notably, $NMC811(OH)_2$ began losing water at a lower temperature than $Ni(OH)_2$, evident from its greater mass loss in the TGA curve and a lower onset temperatures of endothermic events in DSC (250°C vs. 265 °C).

Furthermore, $LiOH·H_2O$ in the mixtures exhibited significantly reduced dehydration temperatures compared to pure $LiOH·H_2O$. In the mixtures, molecular water loss occurred below 90°C and dehydration around 450°C, whereas in pure $LiOH·H_2O$ these events typically occurred near 100°C and above 500°C, respectively. These shifts indicate strong interactions between $LiOH·H_2O$ and $TM(OH)_2$.[47]

In summary, LNO and NMC811 underwent the same four-stage phase evolution during calcination, yet exhibited fundamentally different behaviors in layering and crystallization kinetics:

- **Layering**: In NMC811, the layered phase emerged earlier, coinciding with hydroxide decomposition. This contrasts sharply with LNO, where the onset of layering is markedly delayed until much higher temperatures, highlighting the role of Mn and Co in promoting early layering.
- **Crystallization kinetics**: Despite its early layering, NMC811 exhibited much slower crystallization compared to LNO, pointing to a substitution-induced inhibition of long-range ordering during layered-phase growth.

The dual-phase crystallization process involved a complex interplay of Li/O incorporation, lattice reconstruction, TM oxidation and migration. Importantly, most major peaks, except for $(003)_L$ and $(101)_L$, are shared between the rocksalt and layered phases, reflecting their geometrical correlation. To further resolve the structural ordering and crystallization pathways, Rietveld refinement of the in situ XRD patterns was performed, enabling quantitative comparison between NMC811 and LNO.

3.2 Layering and Crystallization

Beyond the overall transformation from rocksalt to the layered phase, subtle structural evolution can be tracked by changes in lattice parameters, as schematically illustrated in **Figures 2**(a, b). The c/a ratio serves as a key indicator of layered-phase nucleation within the rocksalt framework, while evolution of the rocksalt lattice *a* reflects lithiation dynamics and induced chemical/structural changes. Notably, the rocksalt in NMC811 exhibited a smaller *a* lattice parameter than that of LNO, indicating a higher degree of lithiation. This is attributed to the rapid oxidation of Co^{2+} and Mn^{2+} at low temperatures, which facilitates early lithiation and layered-phase formation.[22] As shown in **Figure 2**(c), lithium accumulated more rapidly in NMC811, with the Li content *x* rising from 0.5 up to 0.85. In contrast, lithiation of rocksalt-LNO was much slower, with *x* remaining below 0.5 due to sluggish Ni oxidation.

At temperatures above ~600 °C, the partially lithiated rocksalt phase in LNO reached a steady state, where the lattice parameter and lithium concentration remained constant over an extended heating period. This behavior reflects a dynamic equilibrium between lithium incorporation into the rocksalt lattice and its concurrent consumption during the layered phase formation. Below ~700 °C, the domain sizes of rocksalt were comparable in NMC811 and LNO; above this temperature, LNO underwent pronounced domain coarsening accompanied by a rapid reduction in rocksalt phase fraction (Figure 1(f)). These observations highlight how lithiation-driven evolution of the rocksalt phase was closely coupled to the crystallization of the layered phase, as further illustrated in **Figure 2**(d).

The difference in layering between NMC811 and LNO is further highlighted by their *c*/*a* ratios at temperatures above 500 °C. During Stage III (below 650 °C), LNO consistently exhibited *c*/*a* values below 4.899, significantly lower than that in NMC811 (4.920), which is due to the highly distorted nanoscale layered domains (< 5 nm) as reported previously.[27] When the layered LNO first emerged, it showed a lower *c* and higher *a* compared to those of the disordered rocksalt (Figure 2(d)). This

anisotropic lattice distortion of the nano-sized LNO, contraction in *c* and expansion in *a*, is attributed to the excess surface energy, specifically enhanced attractive and repulsive interactions along different crystallographic planes.[48]

In general, as the nuclei grow, they progressively lose stability and transition toward a thermodynamically stable state. This happens to the LNO system, where a strong correlation was observed between the *c*/*a* ratio, Li occupancy, and the domain size illustrated in Figure 2(d). Above 650 °C, the domain size in layered LNO grew much faster than in NMC811, indicating more rapid crystallization and Li/TM ordering. The sudden reduction and subsequent recovery of Li content in LNO is likely related to the Li source accessibility: below 740 °C, a fraction of lithium source was trapped in lithium carbonates, becoming inaccessible; as temperature rose above 740 °C, the carbonates started to decompose, releasing lithium. Beyond 800 °C, Li occupancy decreased again due to lithium and oxygen loss at such high temperatures. In contrast, NMC811 maintained a relatively stable Li content up to 800 °C, followed by a gradual decline, which correlates with slower rocksalt-to-layer transformation and delayed crystal growth. Therefore, lithium stoichiometry control during calcination is more challenging in LNO than in NMC811 due to the sluggish lithiation in LNO.[21] Overall, the structural transformation during calcination is governed by an intricate interplay among lithiation, layering, and crystallization. This complexity is further examined through *in situ* PDF analysis.

3.3 Short-range Ordering

The initial nucleation of the layered phase and the rocksalt-to-layer phase transformation involve multiple processes, including dehydration, lithiation, TM oxidation and migration. The resulting structures, especially those associated with disordered phases during hydroxide dehydration cannot be accounted for by Bragg analysis due to their short-range nature. To overcome the limitation and complement the *in situ* XRD analysis, *in situ* PDF measurements were performed to probe local structural changes throughout the transformation from the initial layered TM hydroxides to intermediates and final layered TM oxides.

Figure 3 (a, b) presents temperature-resolved X-ray PDF patterns derived from the Fourier transform of the total scattering data. Consistent with the XRD results, the overall evolution follows four distinct stages:

Stage I: TM hydroxides maintained strong local order, reflecting bulk-like behavior.

Stage II: A sharp drop in structural ordering coincided with hydroxide dehydration and loss of long-range order.

Stage III: New local ordering gradually emerged, marking TM oxide nucleation, with a correlation length of ~5 nm – matching domain sizes from XRD.

Stage IV: Rapid strengthening of local order was observed in both systems, with LNO showing a faster growth rate compared to NMC811.

These observations highlight the role of short-range ordering in mediating the transformation from hydroxides to layered oxides. To further elucidate the relationship between short-range ordering and long-range phase evolution, a quantitative analysis was conducted on the temperature dependence of the peak intensities and positions of the TM-O and TM-TM peaks in NMC811 and LNO, as shown in Figure 3(c) and (d). Peak position reflects atom-pair separations, while peak intensity corresponds to the average coordination number in a defined local volume: the denser the packing density, the higher the peak intensity. In **Stage I**, peak positions were nearly constant, while a gradual decrease in peak intensity was due to the thermal expansion. In **Stage II**, TM-TM distances contracted in both systems, indicating hydroxide dehydration and lattice shrinkage. In NMC811, the TM–O pair distance also contracted, indicating preferential oxidation of Co^{2+}/Mn^{2+} and early lithiation. In contrast, in LNO the Ni–O distance remained nearly constant, indicating that $Ni(OH)_2$ primarily dehydrated without significant Ni oxidation. This divergence explains the delayed layered-phase nucleation in LNO (see Figure 1(f)).

In **Stage III**, Ni-O distances gradually contracted in LNO, consistent with the progressive oxidization of Ni^{2+} to Ni^{3+}. In NMC811, TM-O distance stabilized, suggesting limited TM oxidation. Meanwhile, TM-TM peak intensity displayed a rapid drop in both systems, resulting from the lithiation of rocksalt. Peak intensity dropped due to Li insertion into the lattice, which lowers X-ray scattering.

Overall, PDF analysis reveals that Co/Mn substitution in NMC811 promotes early lithiation and accelerate the nucleation of the layered phase, whereas sluggish Ni oxidation in LNO delays layered-phase formation. These short-range structural signatures further corroborate the distinct transformation pathways between the two systems. Combined XRD and PDF analysis, we can rationalize the differences in the layering and crystallization kinetics between NMC811 and LNO, as summarized in Figure 3(e): in LNO, nucleation of the layered phase is delayed but followed by rapid crystallization; in NMC811, early oxidation of Mn/Co induces prompt nucleation of the layered phase, yet crystal growth is comparatively slower. These contrasting behaviors between NMC811 and LNO are further elucidated through atomistic and mesoscale modeling in the following sections.

3.4 Layering Thermodynamics by Atomistic Modeling

To better understand the distinct lithiation and layering behaviors between NMC811 and LNO (Figures 1(f) and 2), we performed DFT calculations to evaluate the relative stability of the layered and rocksalt phases as a function of Li content (see details in **Note S2** and **Figures S9 and S10**). Our calculations reveal that the rocksalt phase is more energetically favorable at lower levels of lithiation: below 0.65 Li in NMC811 (*i.e.*, $x<0.65$ in $Li_xM_{2-x}O_2$), and 0.80 Li in LNO (**Figure 4**(a-b)). Above these thresholds, the layered phase becomes thermodynamically favorable. In fact, NMC811 requires less lithiation to initiate layering and exhibits greater thermodynamic driving force for this transition than LNO, as evidenced by its lower formation energy (**Figure 4**(c)). It is energetically more favorable for NMC811 to adopt and maintain the layered structure compared to LNO, consistent with the experimental observations of earlier layering in NMC811. These findings provide a mechanistic explanation for the different phase evolution behaviors in the two systems.

The enhanced stability of the layered structure in NMC811 is primarily due to the presence of Mn and Co alongside Ni. As illustrated in **Figure 4**(d), Mn, Co, and Ni tend to form clusters (non-alike nearest neighbors) within the layered framework.

This arrangement leads to a more stable configuration because it maintains an average oxidation state of +3 for the transition metal ions within the cluster. Breaking this stable structure is energetically unfavorable. Therefore, the specific distribution of Mn and Co in NMC811 adds extra stability to the lattice during lithiation.

Despite layered phase being thermodynamically stable in NMC811 at earlier stages of lithiation, the transition from rocksalt to the layered structure is more challenging compared to LNO, most likely due to their different layering mechanisms. Through combined DFT and Ab Initio Molecular Dynamics (AIMD) calculations, we have shown that in LNO the relative gliding between NiO_2 and Li layers is more accessible with low energy cost (See Figure S10 in the SI), consistent with a facile cationic ordering and reduced Li-Ni anti-site formation.[33] In contrast, in NMC811, such a mechanism (gliding) requires more energy and hence limits its contribution to the layering process. As a result, even though the layered phase is energetically favorable, the structural rigidity imposed by Mn and Co delays the transition from the disordered rocksalt to the fully ordered layered phase. This gliding-barrier interpretation represents a mechanistic framework derived from combining DFT and AIMD insights with experimentally observed trends, while acknowledging that direct quantification of kinetic barriers during calcination is experimentally challenging.

3.5 Microstructure Evolution by Mesoscale Modeling

It is evident from the experimental results that along with dehydration, oxidation, lithiation, and layering, the cathode primary particles experience sintering-induced crystallization during calcination.[49] To understand the underlying mass transport processes that occur within the cathode active particles during calcination, computational models at the mesoscale level were developed.[50] Detailed description of the mathematical formulation is provided in **Note S3**. After complete layering, lithium demonstrates high diffusivity within the layered phase.[51] However, at the initial stage of calcination the hydroxide precursors release water and get converted to a rocksalt type structure, which is charactetrizd as the dehydration process.[52] Initial oxidation and lithiation happen within this rocksalt or rocksalt-like transition metal framework, where the diffusivity of oxygen and lithium ions are several orders of magnitude smaller than that observed within the layered phase.[53] Slow lithiation during calcination can be attributed to the fact that both TM oxidation and lithiation need to occur during the calcination process, which can become a challenge in NMC811 and LNO-type cathodes. Also, due to the energy barrier associated with the transition from rocksalt to the layered phase, even after reaching the desired lithium stoichiometry, additional time and energy input may be required for the nucleation and growth of the layered domains. Crystallization of the cathode primary particles can further complicate the scenario by increasing the particle size and, in turn, the diffusion length for ions.

To elucidate the interplay among the dehydration, oxidation, lithiation, layering, and crystallization, a computational model was developed at the mesoscale level to capture the physical phenomena occurring during the calcination of NMC811 and LNO cathode particles (**Note S4**). Comparisons of experimental and atomistic results were conducted to extract the relevant physics to estimate the appropriate model parameters. The influence of the nucleation and propagation of the layered phase within the lithiated rocksalt domain was also incorporated into the computational scheme. The temperature ramp in the model was taken directly from the experiments (as in Figure 1(b)). A change in particle size is observed during calcination due to volume changes from dehydration, oxidation, and lithiation, as well as inter-particle sintering. More specifically, dehydration causes a decrease in particle size (*via* a combination of molar volume reduction and particle cracking), whereas oxidation, lithiation, and sintering lead to an increase in primary particle size – a process identified with crystallization. The potential influence of this crystallization on the chemical reactions and layering of NMC811 and LNO precursors was also investigated. Starting from the transition metal hydroxide precursor microstructure shown in **Figures 5**(a, b)(panel i), both NMC811 and LNO underwent dehydration, oxidation, lithiation, layering, and crystallization at elevated temperatures during the calcination process. Their final particle microstructures and lithium concentration profiles as obtained at around 800°C are shown in Figures 5(a, b)(ii) and 5(a, b)(iii), respectively.

A major structural difference between NMC811 and LNO is the presence of 10% Mn and 10% Co TMs within the Ni matrix, which can influence lithiation, layering, and crystallization dynamics. Slower crystallization for NMC811 results in a final average particle size of 45 nm, whereas LNO reaches an average particle size of 75 – 80 nm at the end of the calcination. The temperature dependent growth in primary particle size is presented in **Figure 5**(c), with black and blue lines representing NMC811 and LNO, respectively. The model shows good agreement with experimental data (circles), obtained by fitting the activation energies associated with the crystallization of the cathode particles in the layered phase.

Irrespective of their crystallization behavior, both NMC811 and LNO experienced complete lithiation towards the end of the calcination, which is clearly denoted by Figures 5(a)(iii) and 5(b)(iii). Prior to lithiation, both the transition metal hydroxide ($NMC811(OH)_2$ and $Ni(OH)_2$) precursors experience dehydration and oxidation of the transition metals. Removal of water from the hydroxide precursors, along with their oxidation, lithiation, and layering are simulated using the developed mathematical framework. The model predicted evolution of different species concentration for NMC811 and LNO is shown in Figures S11(a) and S11(b), respectively, showing similar dehydration of $NMC811(OH)_2$ and $Ni(OH)_2$. The evolution of the oxidized and lithiated species is shown by the overlapping cyan and red lines, respectively (in **Figure S11**). Since oxidation of Mn and Co is easier than that of Ni, NMC811 undergoes faster oxidation and lithiation reactions when LiOH was used as the lithium source. A larger magnitude of reaction rate constant associated with the oxidation process is assumed for NMC811 than LNO to capture their differences in the oxidation and subsequent lithiation process. Direct comparison of the increase in lithium concentration with temperature is shown in **Figure S12** (in the SI section), highlighting earlier lithiation of the NMC811 particles than LNO due to the faster TM oxidation.

The layering process within the lithiated rocksalt domain is modeled as a combination of nucleation and growth of the layered structures.[19] Guided by atomistic simulations, we assume that in pure LNO evolution of the layered phase is possible when the extent of lithiation exceeds a certain threshold ($c_{Li}/c_{Li,max} > 0.3$).[54] On the contrary, NMC811 is assumed to undergo early nucleation of the layered phase due to the presence of Mn and Co, which possibly exist at higher oxidation states

than Ni, consistent with DFT calculations (Figure 4). Computationally predicted layering in LNO and NMC811 cathode particles is plotted in **Figure 5**(d), represented by the black and blue solid lines, respectively. The close agreement with experimental observations (dashed lines) clearly indicates that the layering process is distinctly different from the lithiation. Accordingly, it is treated using a separate governing equation and parameter set (see Eqs. (22) and (23) in SI). Formation and propagation of the layered phase in NMC811 and LNO is denoted by the black line in Figures S11(a) and S11(b) (in the SI), drastically differing from the lithiation phenomenon (red lines).

The nucleation of the layered phase in NMC811 occurred earlier than in LNO (Figure 1(f)) due to the presence of the Mn and Co, which existed at a higher oxidation state than Ni (Mn^{+4} and Co^{+3}). However, the faster nucleation in NMC811 is capped at $x_L \sim 0.3$ by the 10% Mn and 10% Co present, which enables 30% lithiation of the NMC811 cathode particles without requiring Ni oxidation (where x_L denotes extent of layering). The faster oxidation and lithiation of NMC811 possibly contributes to the early layering process. Atomistic simulations further support this mechanism, revealing the formation of stable Ni-Mn-Co honeycomb domains (Figure 4(d)), which aids in the hypothesis of 30% lithiation and layering of NMC811 without any oxidation of Ni^{2+}. On the other hand, the growth of the layered domain in NMC811 is hindered by the presence of Mn and Co, by restricting the interlayer gliding mechanism observed through AIMD simulations. In the mesoscale model, this effect is captured by assigning a lower reaction rate constant associated with the layering process in NMC811 compared to LNO $\left(k_{0,\mathrm{reac,L,NMC811}} < k_{0,\mathrm{reac,L,LNO}}\right)$. **Figures S13**(a, b) demonstrates the evolution of the hydroxide precursor (blue), intermediate rocksalt phase (red), and the layered domains (black) in NMC811 and LNO, respectively. The slower layering kinetics in NMC811 (as compared to LNO) can also be attributed to cation mixing and/or strain effects that are mediated by Mn and Co substitution (**Note S5** and **Figure S14** in SI). During the transition from the RS to the L phase, the RS domain in LNO and NMC811 experiences tensile and compressive strains, respectively. Since the phase change from RS to L is associated with an increase in volume, tensile strains should facilitate the phase change in LNO, whereas, compression should slow it down in NMC811, which is in clear correlation with the experimental observations demonstrated in Figures 1(f) and 5(d).

4. Discussion

Through multiscale-correlated *in situ* characterization and modeling, we demonstrate the critical role of Mn and Co substitutions in regulating the calcination process of Ni-based cathodes. In particular, our study reveals distinct differences in lithiation, layering, and crystallization kinetics between NMC811 and LNO, governed by the complex interplay of thermodynamic and kinetic factors.

– Early lithiation and layering in NMC811: Mn and Co substitutions facilitate early lithiation and layered-phase nucleation in NMC811. DFT calculations show that the layered phase becomes energetically favorable at lower lithium stoichiometry (~0.65 Li) than in LNO (~0.80 Li), promoting earlier nucleation (Figure 4).

– Sluggish crystallization in NMC811: Despite the early layered-phase nucleation, the crystallization in NMC811 is kinetically slower compared to LNO. This is attributed to the increased structural rigidity imposed by Mn and Co substitutions, which raises the energy barrier for interlayer gliding – a critical mechanism for layered-phase propagation. In contrast, in LNO the facile interlayer gliding in homogeneous Ni lattice enables faster crystallization.

Given the 10% Mn and 10% Co content, it can be hypothesized that at least around 30% of the NMC811 lattice structure behaves like $LiNi_{1/3}Mn_{1/3}Co_{1/3}O_2$ (NMC111), forming Ni-Mn-Co honeycomb domains as observed in atomistic simulations (see Figure 4(d)). These domains likely initiate early layered-phase nucleation, which then halts after about 30% conversion, as demonstrated in Figures 1(f) and 5(d). Usually, the kinetic pathways of phase transformation are strongly composition dependent and appear markedly different in the NMC111 compared to NMC811 and LNO. [31, 55] While the presence of the NMC111-like domains in NMC811 is supported by computational modeling, it has not been experimentally confirmed.

Following the early nucleation of the layered domains at low temperatures (< 400°C), their growth mechanism at higher temperatures (> 400°C) becomes the key factors defining the final particle morphology, which can possibly be argued as a kinetically controlled phenomenon. In particular, the growth of the layered domains in NMC811 is much slower than in LNO (shown in Figures 1(f) and 5(d)), which may be justified by the energetics of inter-layer gliding.[33] Complete layering of the transition metal oxide cathode requires gliding of the transition metal and Li layers across the layering plane. The structural stability in the presence of Mn and Co reduces the propensity of interlayer gliding, thus slowing the propagation of the layered phase in NMC811. Conversely, the structural homogeneity in LNO enables more facile gliding and faster layered-phase growth. Crystal-field stabilization analysis suggests that while Co can readily migrate to octahedral sites from a neighboring tetrahedral site, it is hard to move out, making its migration from rocksalt cubic 4a octahedral sites to layer rhombohedral 3a octahedral sites sluggish.[6]

Although both systems undergo an overall similar process, eventually evolving into the thermodynamically favored layered phase, NMC811 follows a different pathway than LNO due to Mn/Co substitution, as illustrated in Figure 6. In LNO, crystallization and structural ordering are sluggish prior to full lithiation and occur mostly during high-temperature sintering when rapid crystal growth sets in (Figures 6 (a); *top*). However, this late-stage growth is accompanied by Li/O loss and structural degradation, making synthetic control of structure and morphology particularly challenging.[21] In contrast, $NMC811(OH)_2$ shows an earlier shift of the $(110)_P$ and $(111)_P$ peaks to higher angles (Figure S6), consistent with early Mn oxidation and formation of the MnOOH phase (with a relatively smaller lattice). This promotes early lithiation and layering and then followed by sluggish crystal growth during high-temperatures sintering (Figure 6a; *bottom*). Consequently, a porous microstructure composed of fine primary particles is formed in calcined NMC811, in contrast to dense, coarse-grained LNO. The distinct interplay between thermodynamics and kinetics may explain the common observations of the smaller particle sizes and enhanced structural stability in NMC811 compared to LNO.

In our current analysis, it is assumed that the presence of Mn and Co slows down the bulk diffusion of transition metal in

NMC811 as compared to LNO, which leads to the lower surface, grain-boundary, and bulk diffusion coefficients, as illustrated in Figure 6 (b). Another important factor is excess Li, which can cause particle fusion through a mechanism called "liquid-phase sintering".[16] Since Mn and Ni substitutions in NMC811 facilitate early lithiation into the lattice (as shown in Figure 2) there is relatively less Li excess than in LNO. As a result, particle fusion occurs more slowly in NMC811. This observation is consistent with a recent report on accelerated interparticle fusion caused by Li excess at grain boundaries.[56] Explicit modeling of the liquid phase sintering process within the mesoscale framework reveals that the reduced activation energy barrier for sintering in LNO is necessary for capturing the rapid grain growth at elevated temperatures (see Note S6 and Figure S15 in SI).

This study focused on the synergistic effects of Mn and Co substitution in the commonly studied NMC811 composition. Atomistic simulations show that incorporating Mn and Co in NMC811 promotes the formation of NMC111-like clusters (Figure 4d), with Mn^{4+}, Co^{3+}, and Ni^{2+} occupying the transition-metal lattice. The strong Mn^{4+}–O^{2-} interaction increases the energetic cost of layer gliding, thereby slowing crystallization in Mn-containing compositions. In contrast, Co^{3+} exhibits ionic interactions with O^{2-} similar to Ni^{3+}, suggesting a limited effect on the crystallization barrier; instead, Co primarily facilitates structural ordering during calcination.[17]

5. Conclusion

This study provides a comprehenaive mechanistic understanding of substitution-mediated calcination thermodynamics and kinetics in Ni-based cathodes. By integrating *in situ* synchrotron measurements, atomistic DFT calculations, and mesoscale modeling, we demonstrate that Mn and Co substitution facilitates early lithiation and layering, while impeding crystallization due to increased energy barriers for interlayer gliding. This decoupling of lithiation and crystallization establishes a mechanistic framework for understand microstructure evolution during the calcination of Ni-based cathodes.

Our findings underscore that targeted elemental substitution, when coupled with tailored temperature profiles, enables predictive control over structure, particle morphology, and ultimately electrochemical performance. The developed multiscale models offer predictive insights into tuning primary particle architecture and size — key factors that influence the cycle life and rate capability of cathodes. Together, these findings establish a general principle for guiding the synthesis of next-generation cathode materials, with improved control over their microstructure and, in turn, electrochemical properties.

ASSOCIATED CONTENT

Supporting Information.
The supporting information is available free of charge via the Internet at http://pubs.acs.org."

The ex situ XRD, SEM for precusors and synthesized NMC811 and LNO and their intermediates, in situ XRD/PDF, PDF data analysis, TGA, DSC measurements, computational results, and related references are provided in Figures S1–S11, Notes S1-S3 and Table S1-3

AUTHOR INFORMATION

[#] *Co-first authors: P.B., S. L;*

**Corresponding authors: F.W.: fengwang@anl.gov; J.B.: jmbai@bnl.gov*

[♦] *K.Z.P. Deceased on May 9, 2025*

Author Contributions

All authors have given approval to the final version of the manuscript.

Notes

The authors declare no competing financial interest.

ACKNOWLEDGMENT

Research at Argonne National Laboratory is supported by the U.S. Department of Energy Office of Energy Efficiency and Renewable Energy Vehicle Technologies Office under Contract No. DE-AC02-06CH11357. Research at Brookhaven National Laboratory is supported by the U.S. Department of Energy Office of Energy Efficiency and Renewable Energy Vehicle Technologies Office under Contract No. DE-SC0012704. Atomistic simulations were performed at the Laboratory Computing Resource Center (LCRC) in Argonne National Laboratory. The baseline precursor materials reported in this paper were synthesized at the Materials Engineering Research Facility (MERF), Argonne National Laboratory. The MERF was supported by the DOE, Office of Energy Efficiency and Renewable Energy, and the Vehicle Technologies Office. This research used the 28-ID-2 (XPD) beamline of the National Synchrotron Light Source II, a DOE Office of Science User Facility operated for the DOE Office of Science by Brookhaven National Laboratory under Contract No. DE-SC0012704.

ABBREVIATIONS

LIB, lithium ion battery; TM, transition metal; XRD, x-ray diffraction; PDF, pair distribution function; NMC811, $LiNi_{0.8}Mn_{0.1}Co_{0.1}O_2$; $LiN_{1/3}Mn_{1/3}Co_{1/3}O_2$ (NMC111), LNO, $LiNiO_2$.

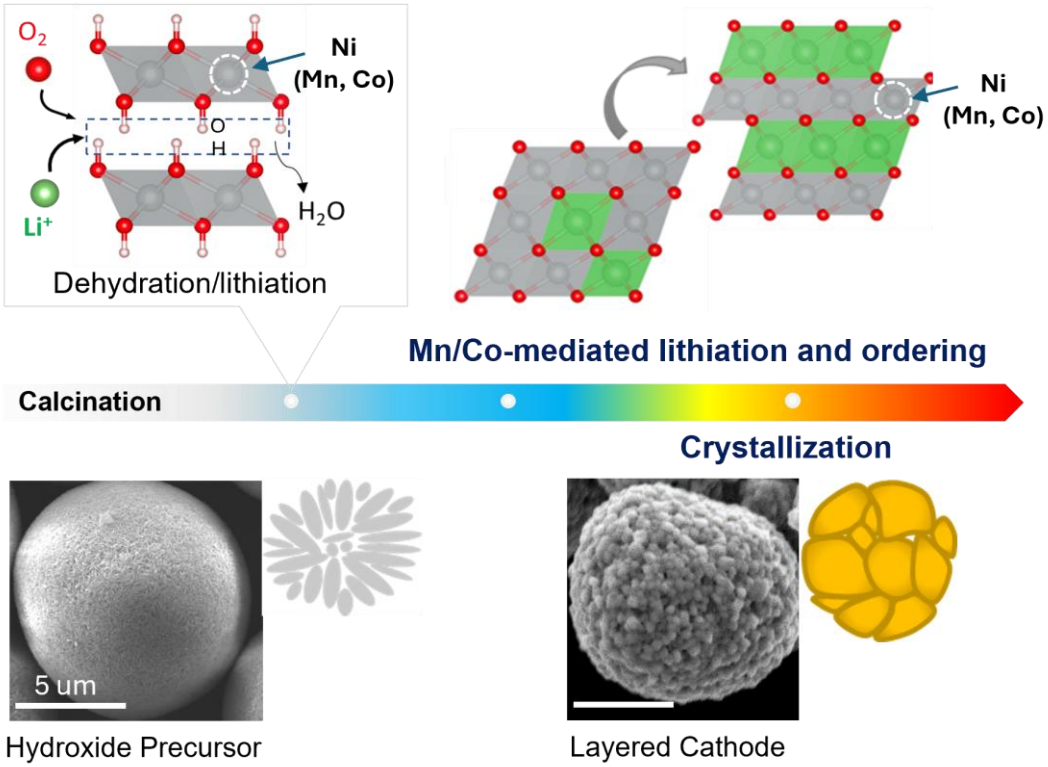

Scheme 1. **Schematic of the substitution-mediated calcination of Ni-based cathodes**, illustrating the transformation from hydroxide precursor (*left*) to layered oxide cathode (*right*), with coupled evolution of structure (top) and morphology (bottom) across multiple length scales.

Top: Concurrent lithiation and dehydration drive a structural transformation from a trigonal structure (S.G.: $P\bar{3}m1$) to a lithiated rocksalt (S.G.: $Fm\bar{3}m$)/layered ($R\bar{3}m$) two-phase composite and eventual conversion to the layered phase.

Bottom: Morphology evolves from the needle-like sub-10 nm-sized primary particles in the hydroxide precursor into ~100 nm primary particles in the layered cathode; during the process, the layered phase nucleates from lithiated intermediates and grows rapidly via sintering-driven coarsening. **Inset**: Schematic illustration of the particle morphology in hydroxide precursors and final layered cathodes.

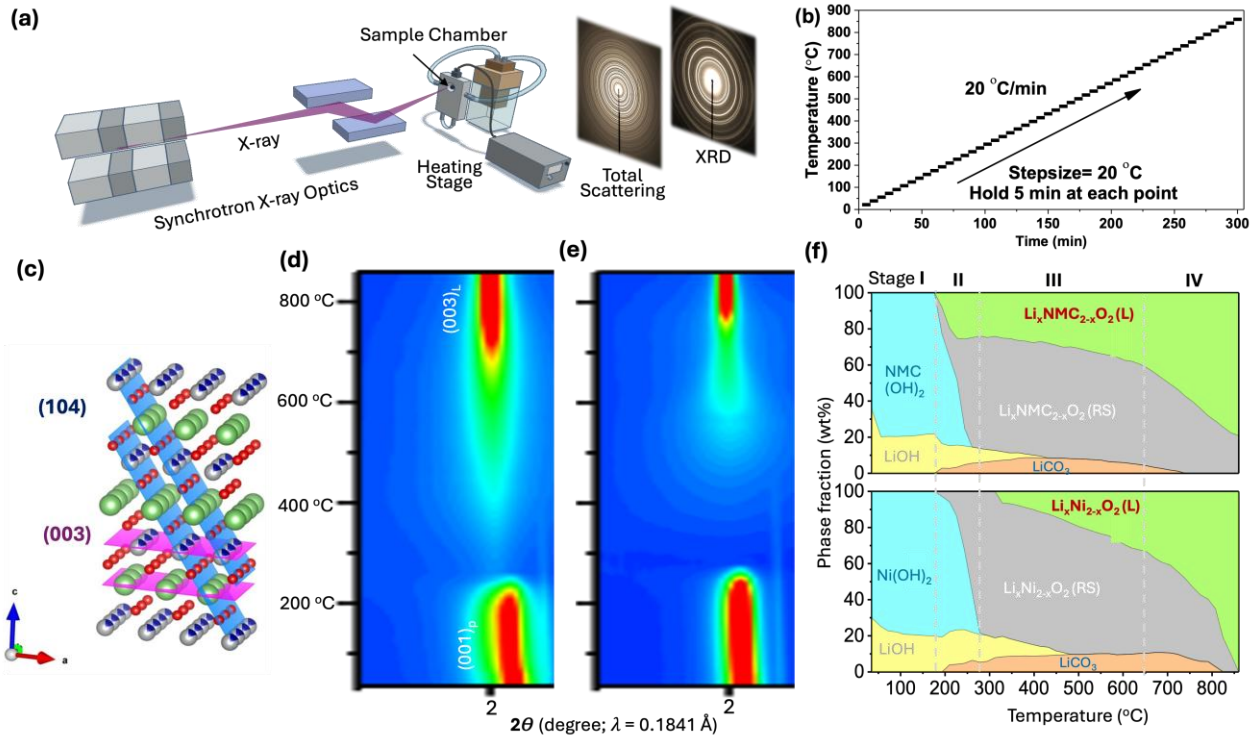

Figure 1. Tracking phase progression and crystallization during the calcination of NMC811 and LNO.

(a) Schematic illustration of the setup for the correlated *in situ* high-energy synchrotron XRD and PDF setup using two CCD detectors, enabling simultaneous data acquisition at the high-angle and low-angle ranges, respectively.

(b) Heating profile for the correlated *in situ* XRD/PDF measurements, with data collected during the 5 min hold at each temperature step.

(c) Atomic configuration of the layered structure with the (104) and (003) lattice planes highlighted in blue and purple, respectively.

(d, e) Contour plots of the temperature-resolved XRD patterns (low angle region) collected during calcination of NMC811 (d) and LNO (e), showing that the hydroxide $(001)_P$ reflection disappears and the layered $(003)_L$ emerges at lower temperatures upon hydroxide decomposition in NMC811 compared with LNO.

(f) Stack plots for the phase fraction (wt%) of the major crystalline phases obtained by Rietveld refinements of the *in situ* XRD data, revealing a shared four-stage pathway with distinct layering and crystallization kinetics:

– **Stage I (RT–180 °C):** hydroxide precursors (P-3m1) remain intact with anisotropic lattice expansion;

– **Stage II (180–280 °C):** dehydration and early lithiation. NMC811 shows faster hydroxide decomposition and the emergence of both layered and rocksalt phases, while LNO delays layered-phase formation until higher temperatures;

– **Stage III (280–650 °C):** ithiated rocksalt $Li_xTM_{2-x}O_2$ gradually transforms into layered $LiTMO_2$. NMC811 exhibits early nucleation early but slower growth, while LNO shows delayed nucleation followed by faster growth;

– **Stage IV (>650 °C):** rapid rocksalt-to-layer transformation. Crystallite growth accelerates in LNO, while NMC811 remains kinetically hindered.

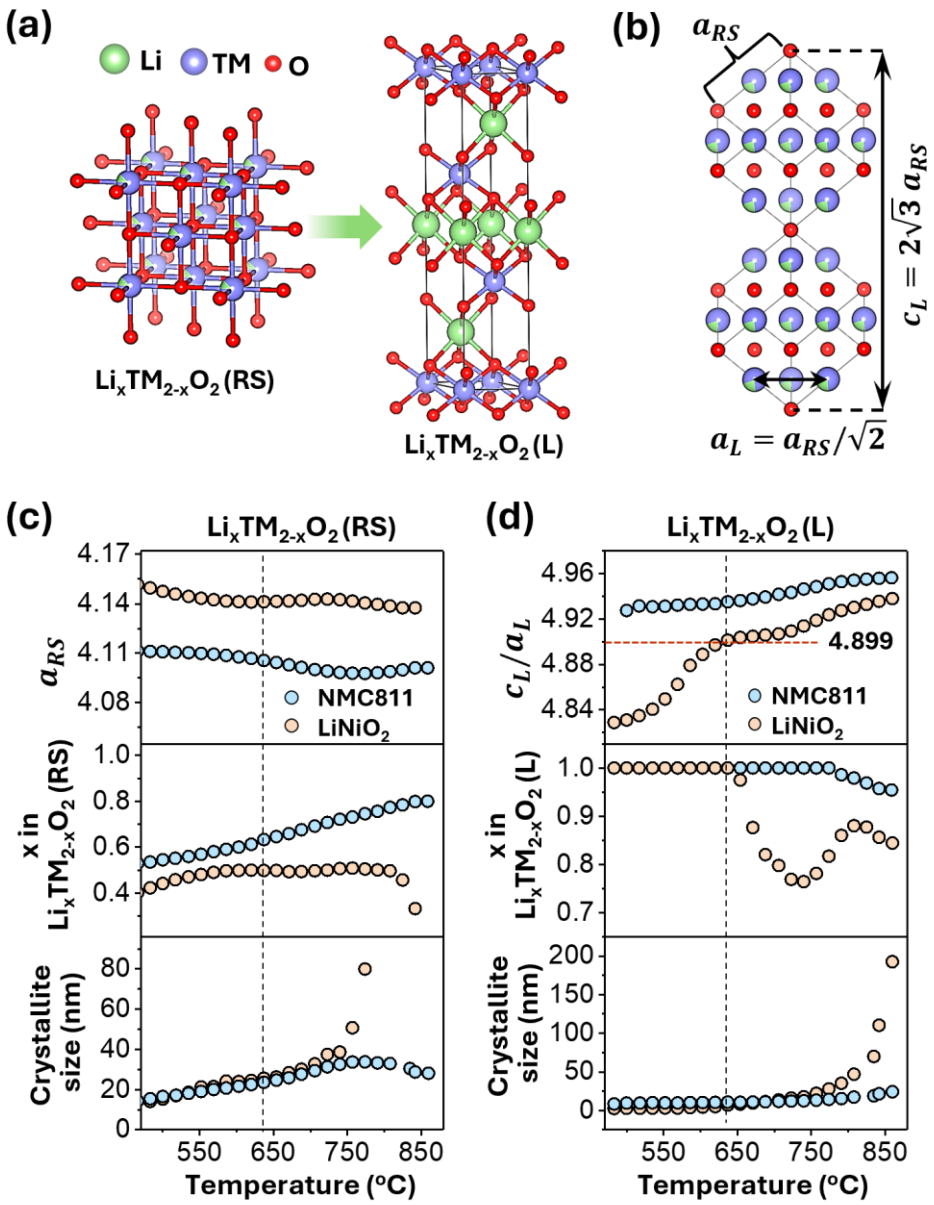

Figure 2. Lithiation-driven structural transformation during calcination of NMC811 and LNO.

(a) Schematic of the rocksalt-to-layer phase transformation.

(b) Correlation between lattice parameters of rocksalt and layered phases, illustrating structural relationships between the two.

(c) Quantitative analysis of structural parameters in the rocksalt phase derived from Rietveld refinement: lattice parameters, lithium occupancy, and domain size

(d) Quantitative analysis of structural parameters in the layered phase obtained from Rietveld refinement: *c*/*a* ratio, lithium occupancy, and domain size

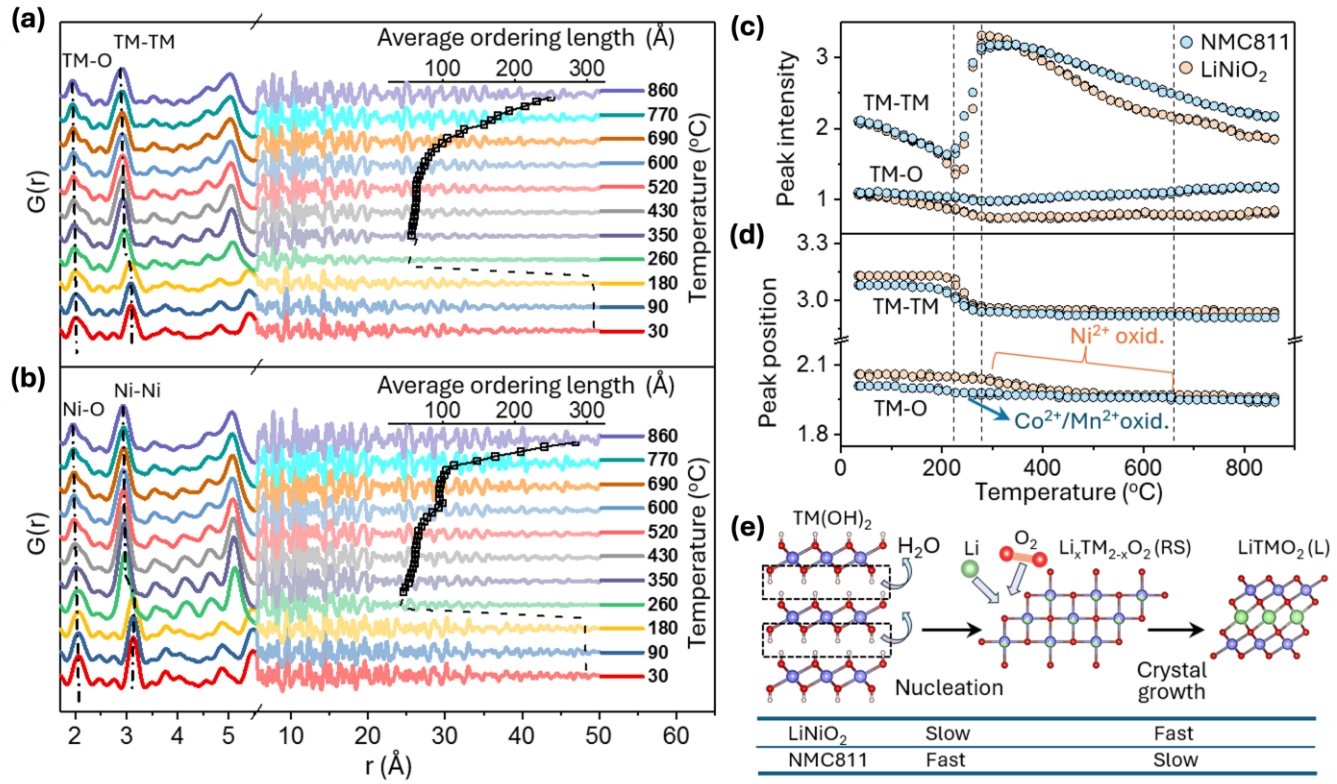

Figure 3. Local structural ordering during calcination of NMC811 and LNO.

(a, b) Temperature-resolved *in situ* PDF patterns over a wide *r* range, showing the evolution of local structural ordering through multiple stages in NMC811 and LNO, respectively.

(c) Integrated intensities of the TM-O (solid circles) and TM-TM (open circles) peaks as a function of temperature.

(d) Peak positions of the TM-O and TM-TM correlations as a function of temperature, reflecting the evolution of the interatomic distances and cation oxidation states across stages.

(e) Schematic comparison of layered-phase nucleation and crystal-growth rates for NMC811 and LNO, highlighting the faster layered-phase nucleation but slower growth in NMC811 (as summarized in the table).

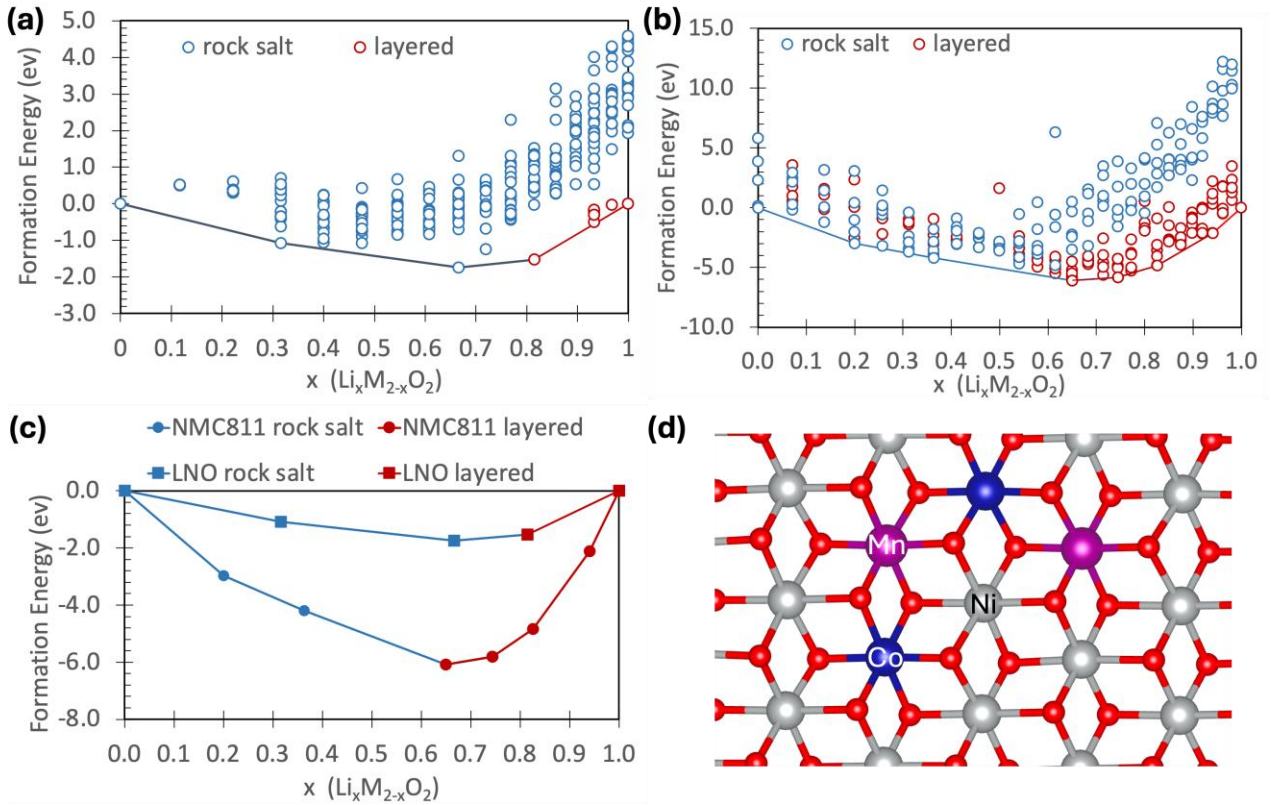

Figure 4. Atomistic insights into layered-phase formation during lithiation.

(a, b) Calculated formation energies of $Li_xM_{2-x}O_2$ as a function of the Li concentration for M = Ni and M=$Ni_{0.8}Mn_{0.1}Co_{0.1}$ respectively. Blue circles represent the disorder rocksalt configurations, where all the elements occupy octahedral sites in a random manner. Red circles represent "layered" configurations, where all the Li ions occupy alternating layers. The blue line is the convex hull representing the equilibrium line where the rocksalt configuration is the more stable. The red line is the convex hull representing the equilibrium line where the layered configuration is the most stable.

(c) Calculated formation energies of $Li_xM_{2-x}O_2$ as a function of the Li concentration. The plot shows the layered configuration becomes thermodynamically favorable at lower Li content for NMC811 (circles) than for LNO (squares).

(d) Ball-and-stick schematic representation of the TM layer (top view) in the layered $Li_xNi_{0.8}Mn_{0.1}Co_{0.1}O_2$, showing the lowest-energy configuration of Ni-Co-Mn clusters.

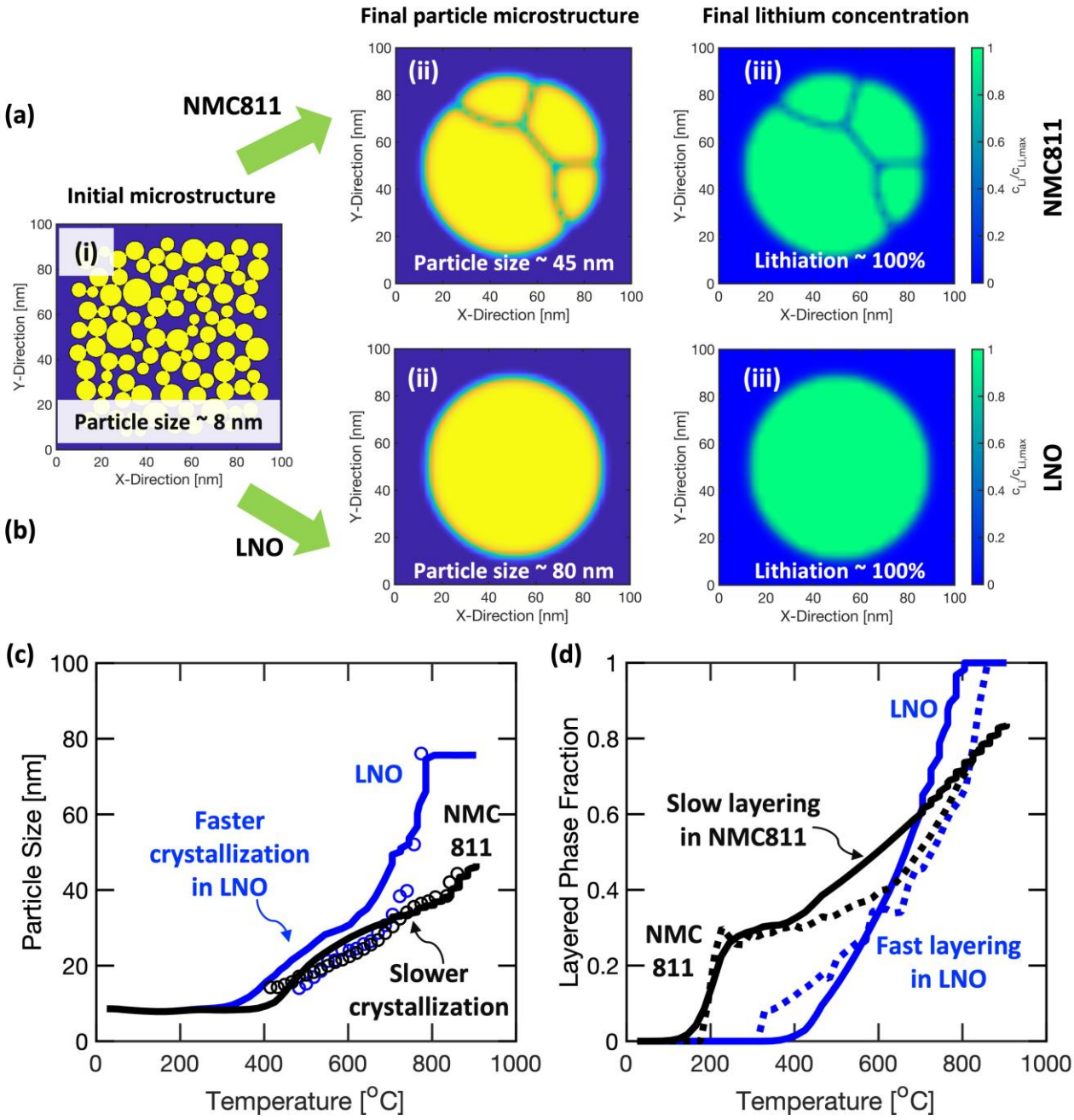

Figure 5. **Mesoscale microstructure evolution and sintering behavior during calcination of NMC811 and LNO.**

(a, b) Particle microstructures and lithiation profiles for NMC811 and LNO, respectively: (i) Initial particle microstructure, (ii) final particle microstructure, and (iii) Li concentration profile at the end of calcination.

(c) Temperature-dependent crystallization in NMC811 and LNO, comparing computational predictions (solid lines) with experimental observations (circles), showing faster crystallization in LNO than in NMC811.

(d) Comparison of the layering process in NMC811 and LNO, showing faster nucleation but slower layered-phase formation in NMC811 than in LNO.

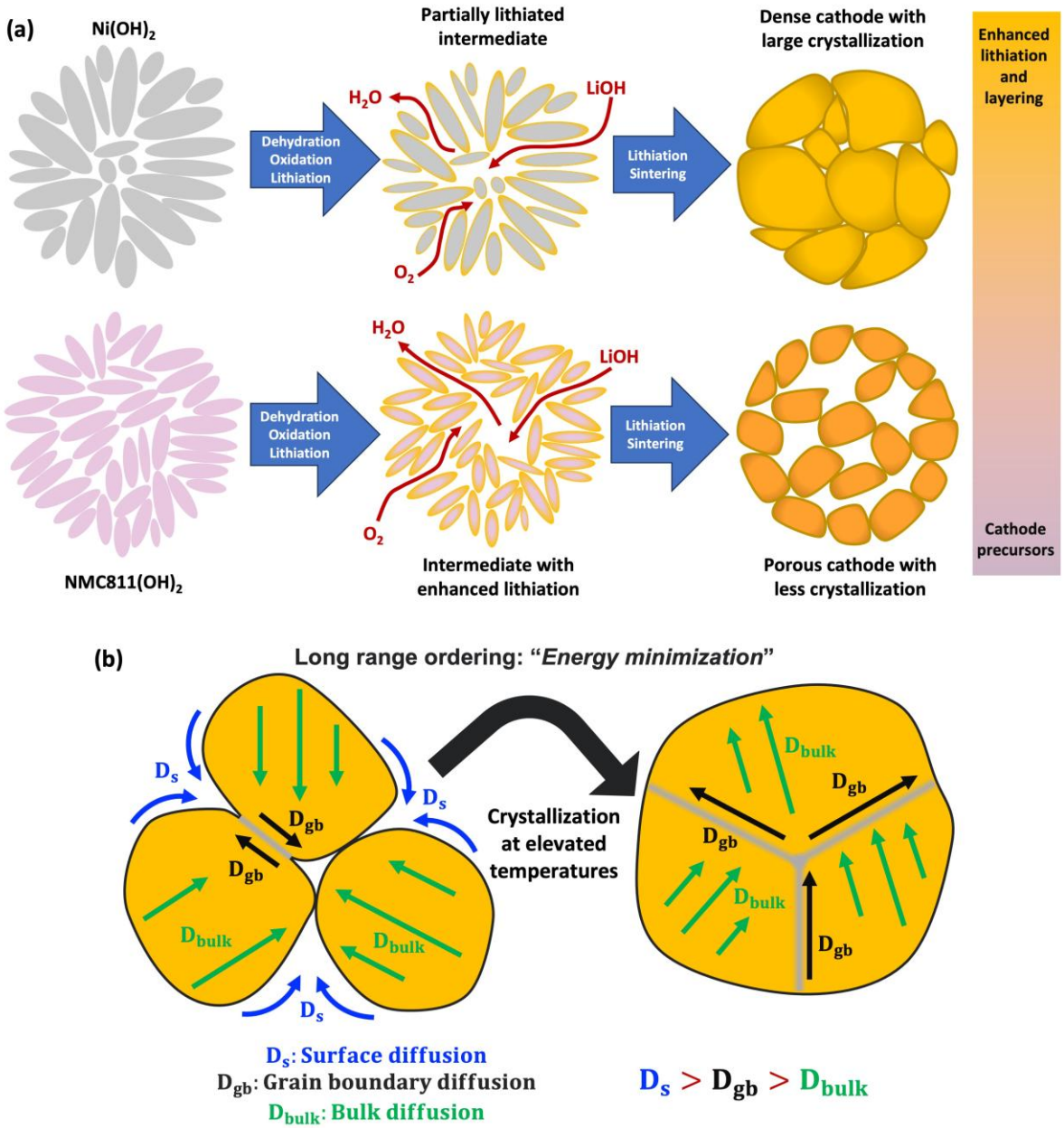

Figure 6. Impact of Mn and Co substitution on microstructure evolution in Ni-based cathodes.

(a) Schematic comparison of the calcination pathways of LNO and NMC811, illustrating differences across the process from early lithiation through layered-phase formation to final crystallization.

(b) Energetics of cathode crystallization at elevated temperatures, illustrating the thermodynamic driving force to reduce total energy by lowering surface energy and the corresponding diffusion mechanisms: surface, grain-boundary, and bulk diffusion that governs crystallization. In general, surface diffusion is fastest, followed by grain-boundary diffusion and then bulk diffusion.

Table of Contents

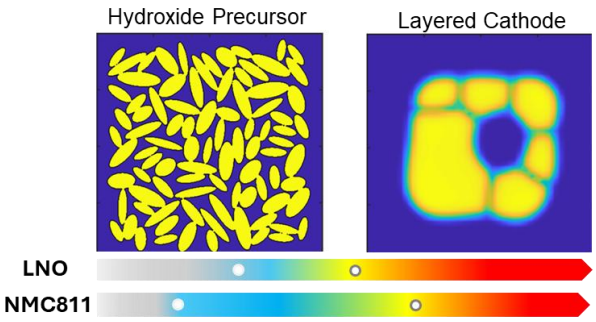

Description (60 words): **Multiscale-correlated experimentation and modeling reveal key insights into nickel-based cathode calcination.** Mn/Co substitution in NMC811 facilitates early lithiation and layered-phase formation while delaying subsequent crystallization – decoupling lithiation and crystallization. This work provides direct evidences explaining contrasting microstructures in NMC811 *versus* $LiNiO_2$ and establishes a mechanistic framework for predictive synthesis of high-performance cathodes.

References

1. Rao, C. N. R.; Cheetham, A. K., Giant Magnetoresistance in Transition Metal Oxides, Science 1996, 272, 369, DOI: 10.1126/science.272.5260.369.
2. Tokura, Y.; Nagaosa, N., Orbital Physics in Transition-Metal Oxides, Science 2000, 288, 462, DOI: 10.1126/science.288.5465.462.
3. Kalinin, S. V.; Spaldin, N. A., Functional Ion Defects in Transition Metal Oxides, Science 2013, 341, 858, DOI: 10.1126/science.1243098.
4. Suntivich, J.; et al. A Perovskite Oxide Optimized for Oxygen Evolution Catalysis from Molecular Orbital Principles, Science 2011, 334, 1383, DOI: 10.1126/science.1212858
5. Whittingham, M. S., Lithium Batteries and Cathode Materials, Chem. Rev., 2004, 104, 4271–4302. https://doi.org/10.1021/cr020731c.
6. Manthiram, A. A Reflection on Lithium-Ion Battery Cathode Chemistry. Nat. Commun. 2020, 11, 1550. https://doi.org/10.1038/s41467-020-15355-0.
7. Goodenough, J. B.; Park, K.-S. The Li-Ion Rechargeable Battery: A Perspective. J. Am. Chem. Soc. 2013, 135, 1167–1176. https://doi.org/10.1021/ja3091438.
8. Lee, S., et al. "Cracking vs. Surface Reactivity in High-nickel Cathodes for Lithium-ion Batteries." *Joule* 2023, 7, 2430-2444. DOI: 10.1016/j.joule.2023.09.006.
9. Yao, J.; et al. Topotaxially grown composite cathodes for cobalt-free high-energy long-life Li-ion batteries. Nat Commun 2025, 16, 10199 https://doi.org/10.1038/s41467-025-63258-9
10. Cui, Z., et al. "Navigating Thermal Stability Intricacies of High-nickel Cathodes for High-energy Lithium Batteries." Nat. Energy 2025, 10, 490–501. https://doi.org/10.1038/s41560-025-01731-x.
11. Kong, F., et al., Kinetic Stability of Bulk $LiNiO_2$ and Surface Degradation by Oxygen Evolution in $LiNiO_2$ - Based Cathode Materials." Adv. Energy Mater. 2019, 91802586. https://doi.org/10.1002/aenm.201802586.
12. Rougier, A., Gravereau, P. and Delmas, C. Optimization of the Composition of the $Li_{1-z}Ni_{1+z}O_2$ Electrode Materials: Structural, Magnetic and Electrochemical Studies, J. Electrochem. Soc. 1996, 143, 1168. **DOI** 10.1149/1.1836614.
13. Wang, F.; et al. Process Design for Calcination of Nickel-Based Cathode Materials by In Situ Characterization and Multiscale Modeling. J. Mater. Res. 2022, 37, 3197–3215. https://doi.org/10.1557/s43578-022-00678-z/
14. Li, W.; Erickson, E. M.; Manthiram, A. High-Nickel Layered Oxide Cathodes for Lithium-Based Automotive Batteries. Nat. Energy 2020, 5, 26–34. https://doi.org/10.1038/s41560-019-0513-0.
15. Zheng, J, et al. "Ni/Li disordering in Layered Transition Metal Oxide: Electrochemical Impact, Origin, and Control." Acc. Chem. Res. 2019, 52, 8, 2201–2209. https://doi.org/10.1021/acs.accounts.9b00033.
16. Liang, C, et al. "Unraveling the Origin of Instability in Ni-rich $LiNi_{1-2x}Co_xMn_xO_2$ (NCM) Cathode Materials." J. Phys. Chem. C 2016, 120, 12, 6383–6393. https://doi.org/10.1021/acs.jpcc.6b00369.
17. Chen, K.; et al. Cobalt-Free Composite-Structured Cathodes with Lithium-Stoichiometry Control for Sustainable Lithium-Ion Batteries. Nat Commun 15, 430 (2024). https://doi.org/10.1038/s41467-023-44583-3.
18. Zhao, J.; et al. In Situ Probing and Synthetic Control of Cationic Ordering in Ni-Rich Layered Oxide Cathodes. Adv. Energy Mater.2017, 7, 1601266. https://doi.org/10.1002/aenm.201601266.
19. Wang, D.; et al. Intrinsic Role of Cationic Substitution in Tuning Li/Ni Mixing in High-Ni Layered Oxides. Chem. Mater. 2019, 31, 2731–2740. https://doi.org/10.1021/acs.chemmater.9b00282.
20. Wang, R.; et al. Tuning Li-Enrichment in High-Ni Layered Oxide Cathodes to Optimize Electrochemical Performance for Li-Ion Battery. Nano Energy, 2019, 62, 709–717. https://doi.org/10.1016/j.nanoen.2019.05.055.
21. Tayal, A.; et al. In Situ Insights into Cathode Calcination for Predictive Synthesis: Kinetic Crystallization of $LiNiO_2$ from Hydroxides. Adv. Mater. 2024, 36, 2312027. https://doi.org/10.1002/adma.202312027.
22. Zhang, M.-J.; et al. Cationic Ordering Coupled to Reconstruction of Basic Building Units During Synthesis of High-Ni Layered Oxides. J. Am. Chem. Soc. 2018, 140, 12484–12492. https://doi.org/10.1021/jacs.8b07464.
23. Park, G.-T.; et al. Unraveling the New Role of Manganese in Nano and Microstructural Engineering of Ni-Rich Layered Cathode for Advanced Lithium-Ion Batteries. Adv. Energy Mater. 2024, 14, 2400130. https://doi.org/10.1002/aenm.202400130.
24. Wang, F.; Bai, J. Synthesis and Processing by Design of High-Nickel Cathode Materials. Batteries Supercaps 2022, 5, e202100174. https://doi.org/10.1002/batt.202100174.
25. Hua, W.; et al. Chemical and Structural Evolution During the Synthesis of Layered $Li(Ni,Co,Mn)O_2$ Oxides. Chem. Mater. 2020, 32, 4984–4997. https://doi.org/10.1021/acs.chemmater.0c00983.
26. Bai, J.; et al. Kinetic Pathways Templated by Low-Temperature Intermediates During Solid-State Synthesis of Layered Oxides. Chem. Mater. 2020, 32, 9906–9913. https://doi.org/10.1021/acs.chemmater.0c03263.
27. Pei, B.; et al. Al Substitution for Mn During Co-Precipitation Boosts the Electrochemical Performance of $LiNi_{0.8}Mn_{0.1}Co_{0.1}O_2$. J. Electrochem. Soc. 2021, 168, 050532. https://doi.org/10.1149/1945-7111/abf8e7.
28. Wang, D.; et al. Synthetic Control of Kinetic Reaction Pathway and Cationic Ordering in High Ni Layered Oxide Cathodes. Adv. Mater. 2017, 29, 1606715. https://doi.org/10.1002/adma.201606715.
29. Cui, Z.; et al. Assessing the Intrinsic Roles of Key Dopant Elements in High-Nickel Layered Oxide Cathodes in Lithium-Based Batteries. Adv. Energy Mater., 2023, 13, 2203853. https://doi.org/10.1002/aenm.202203853.
30. Li, X.; et al. Dopants Modulate Crystal Growth in Molten Salts Enabled by Surface Energy Tuning. J. Mater. Chem. A 2021, 9, 8900–8913. https://doi.org/10.1039/D1TA00001A.
31. Ying, B.; et al. Monitoring the Formation of Nickel-Poor and Nickel-Rich Oxide Cathode Materials for Lithium-Ion Batteries with Synchrotron Radiation. Chem. Mater. 2023, 35, 1514–1526. https://doi.org/10.1021/acs.chemmater.2c03456.
32. Kim, U.-H.; et al. Microstructure Engineered Ni-Rich Layered Cathode for Electric Vehicle Batteries. Adv. Energy Mater. 2021, 11, 2100884. https://doi.org/10.1002/aenm.202100884.
33. Wolfman, M.; et al. Multiscale Insights into Ni-Rich Cathode Synthesis. Adv. Energy Mater. 2022, 12, 2102951. https://doi.org/10.1002/aenm.202102951.
34. Chockalingam, K.; et al. 2D Phase Field Modeling of Sintering of Silver Nanoparticles. Comput. Methods Appl. Mech. Eng. 2016, 312, 492–508. https://doi.org/10.1016/j.cma.2016.09.001.
35. Aryal, S.; et al. Roles of Mn and Co in Ni-Rich Layered Oxide Cathodes Synthesized Utilizing a Taylor Vortex Reactor. Electrochim. Acta 2021, 391, 138929. https://doi.org/10.1016/j.electacta.2021.138929.
36. Proffen, T.; Billinge, S. J. L.; Egami, T.; Louca, D. Structural Analysis Using Diffuse Scattering. Z. Kristallogr. 2003, 218, 132–140. https://doi.org/10.1524/zkri.2003.218.3.132.

37. Whitfield, R. E.; Goossen, D. J.; Welberry, T. R. Diffuse Scattering in Crystalline Materials. IUCrJ 2016, 3, 20. https://doi.org/10.1107/S2052252515023050.
38. Kresse, G.; Furthmüller, J. Efficiency of Ab-Initio Total Energy Calculations for Metals and Semiconductors Using a Plane-Wave Basis Set. Comput. Mater. Sci. 1996, 6, 15–50. https://doi.org/10.1016/0927-0256(96)00008-0.
39. Kresse, G.; Hafner, J. Ab Initio Molecular Dynamics for Liquid Metals. *Phys. Rev. B* 1993, *47*, 558–561. https://doi.org/10.1103/PhysRevB.47.558.
40. Perdew, J. P.; Burke, K.; Ernzerhof, M. Generalized Gradient Approximation Made Simple. *Phys. Rev. Lett.* 1996, *77*, 3865–3868. https://doi.org/10.1103/PhysRevLett.77.3865.
41. Blöchl, P. E. Projector Augmented-Wave Method. *Phys. Rev. B* 1994, *50*, 17953–17979. https://doi.org/10.1103/PhysRevB.50.17953.
42. Garcia, J. C.; ; et al. Surface Structure, Morphology, and Stability of $Li(Ni_{1/3}Mn_{1/3}Co_{1/3})O_2$ Cathode Material. *J. Phys. Chem. C* 2017, *121*, 8290–8299. https://doi.org/10.1021/acs.jpcc.7b00896.
43. Barai, P. and Mukherjee, P. P. Mechano-Electrochemical Stochastics in High-Capacity Electrodes for Energy Storage. *J. Electrochem. Soc.* 2016, 163 A1120. DOI 10.1149/2.01191606jes.
44. Chang, C. C.; Kim, J. Y.; Kumta, P. N. Implications of Reaction Mechanism and Kinetics on the Synthesis of Stoichiometric $LiNiO_2$. J. Electrochem. Soc. 2002, 149, A331–A338. https://doi.org/10.1149/1.1446046.
45. Aykol, M.; Montoya, J. H.; Hummelshøj, J. Rational Solid-State Synthesis Routes for Inorganic Materials. J. Am. Chem. Soc. 2021, 143, 12345–12356. https://doi.org/10.1021/jacs.1c12345.
46. Zheng, J.; et al. Multiscale Insights into Cathode Synthesis. Acc. Chem. Res. 2019, 52, 2201–2210. https://doi.org/10.1021/acs.accounts.9b00201.
47. Jeon, J.; et al. Dehydration Kinetics of the Synthesis of High-Nickel Cathode Materials Used in Lithium-Ion Batteries. J. Mater. Chem. A 2024, 12, 8900–8913. https://doi.org/10.1039/D4TA00001A.
48. Diehm, P. M.; Ágoston, P.; Albe, K. Size-Dependent Lattice Expansion in Nanoparticles: Reality or Anomaly? ChemPhysChem 2012, 13, 2443–2454. https://doi.org/10.1002/cphc.201200245.
49. Noh, M.; Cho, J. Optimized Synthetic Conditions of $LiNi_{0.5}Co_{0.2}Mn_{0.3}O_2$ Cathode Materials for High-Rate Lithium Batteries via Co-Precipitation Method. J. Electrochem. Soc. 2013, 160, A105–A111. https://doi.org/10.1149/2.105301jes.
50. Dong, H. X.; Wang, A.; Koenig, G. M. Role of Coprecipitation and Calcination of Precursors on Phase Homogeneity and Electrochemical Properties of Battery Active Materials. Powder Technol. 2018, 335, 137–146. https://doi.org/10.1016/j.powtec.2018.05.001.
51. Yang, S.; et al. Temperature-Dependent Lithium-Ion Diffusion and Activation Energy of $Li_{1.2}Co_{0.13}Ni_{0.13}Mn_{0.54}O_2$ Thin-Film Cathode at Nanoscale by Using Electrochemical Strain Microscopy. ACS Appl. Mater. Interfaces 2017, 9, 13999–14005. https://doi.org/10.1021/acsami.7b03245.
52. Bianchini, M.; et al. An In Situ Structural Study on the Synthesis and Decomposition of $LiNiO_2$. J. Mater. Chem. A 2020, 8, 1808–1820. https://doi.org/10.1039/C9TA00001A.
53. Lin, F.; et al. Surface Reconstruction and Chemical Evolution of Stoichiometric Layered Cathode Materials for Lithium-Ion Batteries. Nat. Commun. 2014, 5, 1–10. https://doi.org/10.1038/ncomms12345.
54. Das, H.; et al. First-Principles Simulation of the (Li-Ni-Vacancy)O Phase Diagram and Its Relevance for the Surface Phases in Ni-Rich Li-Ion Cathode Materials. Chem. Mater. 2017, 29, 7840–7851. https://doi.org/10.1021/acs.chemmater.7b03456.
55. Kinnibrugh, Tiffany L., et al. "Thermodynamic and Kinetic Mechanisms Governing the Synthesis of Nickel-Poor Cathodes." Chem. Mater., 2025, 37, 6256-6270. https://doi.org/10.1021/acs.chemmater.5c01173.
56. Qiu, L.; et al. Origin and Regulation of Interface Fusion During Synthesis of Single-Crystal Ni-Rich Cathodes. Angew. Chem. Int. Ed.2023, 62, e202300209. https://doi.org/10.1002/anie.202300209.